Draft version February 20, 2012
Preprint typeset using LaTeX style emulateapj v. 02/07/07

A DENSITY INDEPENDENT FORMULATION OF SMOOTHED PARTICLE HYDRODYNAMICS

Takayuki R.Saitoh[1] & Junichiro Makino[1]

Draft version February 20, 2012

ABSTRACT

In the standard formulation of the smoothed particle hydrodynamics (SPH), it is assumed that the local density distribution is differentiable. This assumption is used to derive the spatial derivatives of other quantities. However, this assumption breaks down at the contact discontinuity, which appears often in simulations of astronomical objects. At the contact discontinuity, the density of the low-density side is overestimated while that of the high-density side is underestimated. As a result, the pressure of the low (high) density side is over (under) estimated. Thus, unphysical repulsive force appears at the contact discontinuity, resulting in the effective surface tension. This effective surface tension suppresses instabilities such as the Kelvin-Helmholtz and Rayleigh-Taylor instabilities. In this paper, we present a new formulation of SPH, which does not require the differentiability of density and thus can handle contact discontinuity without numerical problems. The results of standard tests such as the shock tube, Kelvin-Helmholtz and Rayleigh-Taylor instabilities, and the blob tests are all very favorable to our new formulation. We conclude that our new formulation solved practically all known difficulties of the standard SPH, without introducing additional numerical diffusion or breaking the exact force symmetry or energy conservation.

Subject headings: galaxies:evolution—galaxies:ISM—methods:numerical

1. INTRODUCTION

Smoothed particle hydrodynamics (SPH) is a lagrange scheme to solve the evolution of fluid using particles. It was originally introduced by Lucy (1977) and Gingold & Monaghan (1977) and has been widely used in the field of the computational astrophysics (Monaghan 1992, 2005; Rosswog 2009; Springel 2010b). It is becoming popular in hydrodynamical simulations in engineering (e.g., Liu & Liu 2003).

Recently, Agertz et al. (2007) reported the results of comparison of SPH and Euler schemes (grid methods). Their main result is that SPH suppresses the Kelvin-Helmholtz instability. This has been pointed out by Okamoto et al. (2003). The reason of this problem is that in the standard SPH the smoothed density is used to obtain other physical quantities. The estimated density of particles near the contact discontinuity has $\mathcal{O}(1)$ error, irrespective of the numerical resolution. This large error causes similarly large error in the pressure (see §2). Agertz et al. (2007) noted that there were *fundamental differences* between SPH and grid methods.

There have been several proposals to improve SPH so that it can deal with the contact discontinuity. Price (2008) discussed the artificial thermal conductivity which was originally introduced by Monaghan (1997). The motivation of the use of the artificial conductivity is that every physical quantity should be *smooth* in the standard SPH. The artificial conductivity eliminates the discontinuity in the thermal energy. As a result, the density near the contact discontinuity becomes smooth and the pressure also becomes smooth with this artificial conductivity. Thus, the Kelvin-Helmholtz instability takes place. At the first sight, this artificial conductivity looks similar to the artificial viscosity which is necessary to capture shocks in SPH. However, there are two fundamental differences. First, the artificial viscosity is used to generate the physical dissipation associated with the shock, while the artificial conductivity adds physically non-existent dissipation. One needs to fine-tune the conductivity coefficient to prevent unnecessary smoothing. This means that the conductivity must be non-linear. Second, if there is a jump in the chemical composition, thermal conductivity is not enough. However, whether the use of artificial chemical diffusion is justified or not is an open question. Read et al. (2010) suggested that the Kelvin-Helmholtz instability took place when the number of neighbors was sufficiently large and the momentum equation of the Ritchie & Thomas (2001) was used. Abel (2011) used the relative pressure instead of the absolute values of pressures in the equation of motion. This formulation improves the treatment of the Kelvin-Helmholtz instability, but breaks the Newton's third law. García-Senz et al. (2012) considered the use of the integral form of the first derivative, which also improved the treatment of hydrodynamical instabilities.

In this paper, we describe a new formulation of SPH which does not use the smoothed mass density. Instead, we use the smoothed internal energy density to obtain other quantities and their spatial derivatives. The reason why we adopt the energy density instead of the mass density is that it is the fundamental quantity of the hydrodynamics. In our formulation, the pressure is calculated without using the mass density. Thus, unphysical jumps of pressure at the contact discontinuity disappear. Our equation of motion is similar to that of Ritchie & Thomas (2001), although the basis of deviation is completely different. Results of various tests indicate that our formulation is highly advantageous.

The structure of this paper is as follows. In §2, we analyze the problem of standard SPH at discontinuities. Our new formulation of SPH is described in §3 and the comparison of the results of test calculations with the

Electronic address: saitoh@geo.titech.ac.jp
[1] Interactive Research Center of Science, Tokyo Institute of Technology, 2–12–1, Ookayama, Meguro, Tokyo, 152-8551, Japan

new formulation and standard formulation are shown in §4. Summary and discussion are presented in §5.

2. STANDARD SPH AND ITS DIFFICULTY AROUND DISCONTINUITIES

In SPH, the fluid is expressed by discrete particles and physical quantities are approximated by kernel interpolation. In the standard formulation of SPH, the local density is first calculated, and then the rests of necessary physical quantities, such as the pressure gradient and the time derivative of the internal energy, are calculated. Thus, the accuracy of the solution depends on the accuracy of the density estimate. In this section, we re-examine the derivation of the equation of motion in SPH to understand its problem.

A physical quantity f at position $\boldsymbol{r}$ can be expressed as follows:

$$f(\boldsymbol{r}) = \int f(\boldsymbol{r}')\delta(|\boldsymbol{r}-\boldsymbol{r}'|)d\boldsymbol{r}'. \tag{1}$$

A smoothed value of f at position $\boldsymbol{r}$, $\langle f\rangle(\boldsymbol{r})$, is given by the convolution of f and a kernel function $W(\boldsymbol{r}-\boldsymbol{r}', h)$:

$$\langle f\rangle(\boldsymbol{r}) = \int f(\boldsymbol{r}')W(|\boldsymbol{r}-\boldsymbol{r}'|, h)d\boldsymbol{r}', \tag{2}$$

where h is the size of the kernel function and corresponds to the spatial resolution. This smoothing is the base of SPH. Here, the kernel function must satisfy the following three conditions: (1) it becomes the delta function in the limit of $h \to 0$, (2) it is normalized as unity, and (3) it is a function with compact support. A cubic spline function is most widely used as the kernel function:

$$W(|\boldsymbol{r}-\boldsymbol{r}'|, h) = \frac{\sigma}{h^D}\begin{cases}\left(1-\frac{3}{2}s^2+\frac{3}{4}s^3\right) & 0 \le s < 1,\\ \frac{1}{4}(2-s)^3 & 1 \le s < 2,\\ 0 & 2 \le s,\end{cases} \tag{3}$$

where $s = |\boldsymbol{r}-\boldsymbol{r}'|/h$, D is the dimension, and the normalized factors σ in one, two, and three dimensions are $2/3$, $10/7\pi$, and $1/\pi$, respectively. We first derive the equations of motion and energy with the constant kernel size, and then we generalized them to the individual kernel size.

The first derivative of the smoothed f is given by

$$\langle \nabla f\rangle(\boldsymbol{r}) = \int \nabla f(\boldsymbol{r}')W(|\boldsymbol{r}-\boldsymbol{r}'|, h)d\boldsymbol{r}'. \tag{4}$$

By making use of the partial integral and the fact that the kernel function has compact support, Eq. 4 becomes

$$\langle \nabla f\rangle(\boldsymbol{r}) = \int f(\boldsymbol{r}')\nabla W(|\boldsymbol{r}-\boldsymbol{r}'|, h)d\boldsymbol{r}'. \tag{5}$$

We need to discretize Eq. 2 to evaluate the physical quantities at positions of particles. To convert integral into summation, a volume element $d\boldsymbol{r}'$ is replaced by m_j/ρ_j, where m_j and ρ_j are the mass and density of the particle j. In addition, positions of particles i and j are expressed by $\boldsymbol{r}_i$ and $\boldsymbol{r}_j$ and $f(\boldsymbol{r}')$ is replaced by f_j. Thus, the value of f at the position of particle i is

$$\langle f\rangle(\boldsymbol{r}_i) \simeq \sum_j m_j \frac{f_j}{\rho_j} W(r_{ij}, h), \tag{6}$$

where $r_{ij} = |\boldsymbol{r}_{ij}|$ and $\boldsymbol{r}_{ij} = \boldsymbol{r}_i - \boldsymbol{r}_j$. Hereafter, we call the SPH formulation with this type of discretization as the *standard SPH*. At this point, we do not know ρ_j. By substituting ρ into f, we obtain

$$\rho_i \simeq \sum_j m_j W(r_{ij}, h), \tag{7}$$

where $\rho_i \equiv \langle\rho\rangle(\boldsymbol{r}_i)$ is the smoothed density at the position of particle i. Note that the right-hand side of Eq. 7 includes no unknown quantities. Thus, densities should be calculated first in the standard SPH.

The equation of motion is

$$\frac{d^2\boldsymbol{r}}{dt^2} = -\frac{\nabla P}{\rho}, \tag{8}$$

where t is time and P is pressure. The SPH approximation of Eq. 8 is given by

$$\frac{d^2\boldsymbol{r}_i}{dt^2} \simeq -\sum_j m_j \left(\frac{P_i}{\rho_i^2} + \frac{P_j}{\rho_j^2}\right)\nabla W(r_{ij}, h). \tag{9}$$

This form satisfies the Newton's third law. We used the following relation to obtain Eq. 9:

$$\frac{\nabla P}{\rho} = \nabla\left(\frac{P}{\rho}\right) - \frac{P}{\rho^2}\nabla\rho. \tag{10}$$

In order for Eq. 9 to be meaningful, ρ must be differentiable, since its derivative is used in Eq. 10.

Finally, we derive the energy equation in the standard SPH. The energy equation is

$$\frac{du}{dt} = -\frac{P}{\rho}\nabla\cdot\boldsymbol{v}, \tag{11}$$

where u is the internal energy and $\boldsymbol{v}$ is the velocity. To obtain the SPH formulation of the energy equation, we need the SPH expression of $\nabla\cdot\boldsymbol{v}$. We use

$$\nabla(\rho\boldsymbol{v}) = \nabla\rho\boldsymbol{v} + \rho\nabla\cdot\boldsymbol{v}. \tag{12}$$

The SPH formulation of $\nabla\cdot\boldsymbol{v}$ is given by

$$\begin{aligned}\rho_i\nabla\cdot\boldsymbol{v}_i &\simeq \sum_j m_j\boldsymbol{v}_j\cdot\nabla W(r_{ij}, h) - \boldsymbol{v}_i\cdot\sum_j m_j\nabla W(r_{ij}, h)\\ &= -\sum_j m_j\boldsymbol{v}_{ij}\cdot\nabla W(r_{ij}, h),\end{aligned} \tag{13}$$

where $\boldsymbol{v}_{ij} = \boldsymbol{v}_i - \boldsymbol{v}_j$. Therefore, the energy equation in the standard SPH is

$$\frac{du_i}{dt} \simeq \sum m_j\frac{P_i}{\rho_i^2}\boldsymbol{v}_{ij}\cdot\nabla W(r_{ij}, h). \tag{14}$$

Equations 7, 9, and 14 close with the equation of state (EOS),

$$P = (\gamma-1)\rho u, \tag{15}$$

where γ is the specific heat ratio. There is no need to solve the continuity equation in SPH since it is satisfied automatically.

When we use the variable and individual kernel size, above equations should be modified slightly. First, the density evaluation equation is rewritten as

$$\rho_i \simeq \sum_j m_j W(r_{ij}, h_i). \tag{16}$$

This is the so-called gather interpretation of the summation (Hernquist & Katz 1989). In equations of motion

and energy, the gather-and-scatter interpretation is used (Hernquist & Katz 1989). Thus, Eqs. 9 and 14 become

$$\frac{d^2\boldsymbol{r}_i}{dt^2} \simeq -\sum_j m_j \left(\frac{P_i}{\rho_i^2} + \frac{P_j}{\rho_j^2}\right) \nabla \tilde{W}_{ij}, \tag{17}$$

and

$$\frac{du_i}{dt} \simeq \sum_j m_j \frac{P_i}{\rho_i^2} \boldsymbol{v}_{ij} \cdot \nabla \tilde{W}_{ij}, \tag{18}$$

where $\nabla W(r_{ij}, h_i)$ is replaced by $\nabla \tilde{W}_{ij} = 0.5[\nabla W(r_{ij}, h_i) + \nabla W(r_{ij}, h_j)]$ so that the equation of motion can satisfy the Newton's third law. It is also possible to use $\nabla \tilde{W}_{ij} = \nabla W[r_{ij}, 0.5(h_i + h_j)]$. We adopt the first form throughout this paper.

In the derivation of the standard SPH discretization, the differentiability of ρ is used for both the equation of motion and the energy equation. However, ρ is discontinuous at the contact discontinuity. In the following, we illustrate the consequence of the discontinuity of the density.

In Figure 1, we show the values of density and pressure around a contact discontinuity evaluated by the standard formulation of SPH. Equation 16 is used and $P = (\gamma - 1)\rho u$. To set up this contact discontinuity, we place particles on a regular grid in three dimensions and set $\rho = 1$ for $x < 0.5$ and $\rho = 0.125$ for $x > 0.5$. We used equal-mass particles in the first two configurations. In these two setups, positions of particles in the less dense region is determined by taking the center of mass of the eight particles in the cube of the particle separation. In the last configuration, we adopted the equal separation for both regions, which means that the mass of particles in the less dense region is 1/8 of that of particles in the dense region. The internal energy was set to 1.5 ($x < 0.5$) and 12 ($x > 0.5$), and the specific heat ratio was 5/3. Velocities of particles were set to zero. The kernel size is determined to keep the neighbor number, $N_{\rm nb}$, to the range 32 ± 2, in the first and the last tests. In the second test a constant h fixed to twice the particle separation in the less dense region is used.

The top panels show the distribution of particles. The panels in the second row show the SPH density. Though the initial setup has the discontinuity at $x = 0.5$, it is smoothed by the kernel. As a result, SPH density of particles next to the discontinuity has very large errors, as shown in the 3rd row. This large error in the density causes similarly large error in the pressure (4th row). The pressure of particles at the end of the low-density region is grossly overestimated, while that at the end of the high-density region is underestimated only modestly. This non-symmetric error in the pressure is the origin of the repulsive force at the contact discontinuity, as has been pointed out in previous studies (e.g., Ritchie & Thomas 2001; Okamoto et al. 2003; Agertz et al. 2007). This large error in the pressure also exists in both of the constant kernel size case (the middle column) and the equal-separation case (the right column).

Consider the following density and pressure distribution:

$$\rho = \begin{cases} \rho_1 & x \geq 0, \\ \rho_2 & x < 0, \end{cases} \tag{19}$$

and

$$P = P_0. \tag{20}$$

Obviously, we have

$$\langle \rho \rangle(x) \to \frac{\rho_1 + \rho_2}{2}, \quad \text{for } x \to 0, \tag{21}$$

and therefore,

$$\lim_{x \to +0} \langle P \rangle(x) = \frac{\rho_1 + \rho_2}{2\rho_1} P_0, \tag{22}$$

$$\lim_{x \to -0} \langle P \rangle(x) = \frac{\rho_1 + \rho_2}{2\rho_2} P_0. \tag{23}$$

Thus, if $\rho_1 \ll \rho_2$, the error of the pressure can be arbitrarily large. Note that the existence of this error does not imply the inconsistency of SPH. In this limit of $h \to 0$, the volume of the regime affected by this error approaches to zero, which means the original differential equation is restored almost everywhere. In other words, SPH satisfies the weak form of the original equation. However, it means the convergence is slow and first order.

One might think that this error is caused by an inadequate initial thermal energy distribution. However, it is not the case. Even if we initialize the internal energy of particles near the contact discontinuity so that pressure is smooth, the particle distribution changes and discontinuity is regenerated. We, thus, need continuous adjustment to suppress the pressure error throughout the time integration. Price's artificial conductivity (Price 2008) provides such a continuous adjustment. Though the artificial conductivity works beautifully in test calculations for the Kelvin-Helmholtz instability, whether its use in actual astrophysical simulation is justified or not is a bit questionable. First, in the case of the discontinuity of chemical composition, not only the jump in the internal energy but also that in the chemical composition should be smoothed but that is clearly not adequate. Second, the artificial heat conduction can significantly enhance the thermal relaxation of the system, which is again unwanted.

3. A DENSITY INDEPENDENT FORMULATION OF SPH

In §2, we have seen that the standard SPH breaks down at the contact discontinuity because the continuity and differentiability of the density is necessary to guarantee the convergence of SPH approximation. The basic reason for this problem is the use of mj/ρ_j as the volume element. Thus, if we use something else as the volume element, we might be able to avoid this difficulty altogether.

3.1. *Concept*

Here, we propose an alternative formulation of SPH in which we discretize Eq. 2 using the EOS of fluid, not the mass density. The new volume element is

$$d\boldsymbol{r}' = \frac{(\gamma - 1) m_j u_j}{P_j}. \tag{24}$$

Substituting Eq. 24 into Eq. 2 and using the gather summation, we obtain a new SPH approximation of smoothed f:

$$\langle f \rangle(\boldsymbol{r}_i) \simeq \sum_j (\gamma - 1) \frac{m_j u_j f_j}{P_j} W(r_{ij}, h_i), \tag{25}$$

$$= \sum_j (\gamma - 1) \frac{U_j f_j}{P_j} W(r_{ij}, h_i), \tag{26}$$

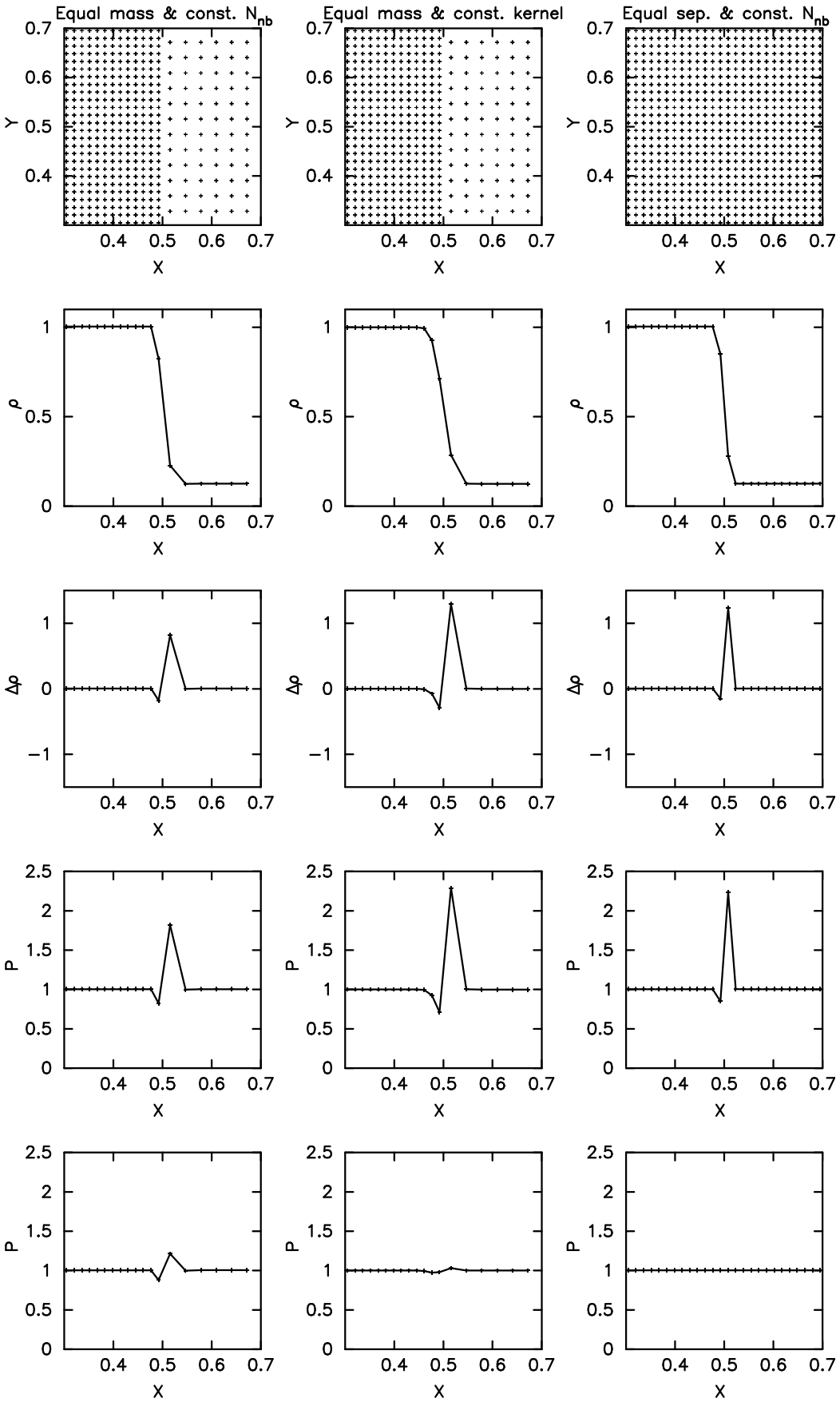

FIG. 1.— Density and pressure fields evaluated with the standard SPH and our new SPH around the contact discontinuity with the density ratio of 1 : 8. Equal mass particles are used for the first and second configurations (the left and middle columns). The positions of the less dense region is determined by taking the center of mass of the eight particles in the cube of the particle separation. The equal separation is used in the last configuration (the right column). In this configuration, the mass of particles in the less dense region is 1/8 of that of particles in the dense region. For the left and right columns, the constant neighbor number, 32 ± 2, is used. In the middle column, a constant kernel size of 0.03125 is used. The top row shows the distribution of particles projected on the $x - y$ plane. The second row shows the density of each SPH particle evaluated with Eq. 16. The third row shows the density contrast between the evaluated density and true one. The fourth row shows corresponding pressure. In the bottom row, the pressure of each particle calculated with our new SPH is shown.

where $U_i = m_i u_i$ is the internal energy of particle i. By substituting f with the energy density, $q \equiv \rho u$, we have

$$q_i \simeq \sum_j U_j W(r_{ij}, h_i). \tag{27}$$

where we used $q_i \equiv \langle q \rangle(\boldsymbol{r})$. The gradient of $\langle f \rangle$ is given by

$$\langle \nabla f \rangle(\boldsymbol{r}_i) \simeq \sum_j U_j \frac{f_j}{q_j} \nabla W(r_{ij}, h_i). \tag{28}$$

We adopt Eqs. 26 and 27 as the basis of our new formulation. We derive the equations of motion and energy from this basis. We note that our new SPH is also Galilei invariant.

One might think that the use of U for the calculation of the volume element would cause some inconsistency, since U is not a conserved quantity. The mass of a particle is constant, and thus looks safer. In the following, we show that we can construct a consistent set of equations using U, and that it has many advantages over the standard SPH and that it retains important characteristics such as force symmetry and energy conservation. We first derive the energy equation and then equation of motion. We then discuss the formulation for the estimate of the density and the implementation of the artificial viscosity.

3.2. *Energy Equation*

We need an expression of $\nabla \cdot \boldsymbol{v}$ to derive the energy equation. We start with

$$\nabla(q\boldsymbol{v}) = \nabla q \boldsymbol{v} + q \nabla \cdot \boldsymbol{v}, \tag{29}$$

which is obtained by replacing ρ in Eq. 12 by q. By applying Eq. 28 to Eq 29, we obtain an analogy of Eq. 13:

$$\begin{aligned} q_i \nabla \cdot \boldsymbol{v}_i \simeq & \sum_j U_j \boldsymbol{v}_j \cdot \nabla W(r_{ij}, h_i) - \boldsymbol{v}_i \cdot \sum_j U_j \nabla W(r_{ij}, h_i) \\ = & -\sum_j U_j \boldsymbol{v}_{ij} \cdot \nabla W(r_{ij}, h_i). \end{aligned} \tag{30}$$

The energy equation is then given by

$$\frac{du_i}{dt} \simeq \sum_j U_j \frac{P_i}{\rho_i q_i} \boldsymbol{v}_{ij} \cdot \nabla \tilde{W}_{ij}. \tag{31}$$

Equation 31 contains ρ_i since u is the energy per unit mass. The equation for U_i is obtained by multiplying Eq. 31 by m_i:

$$\frac{dU_i}{dt} \simeq \frac{m_i}{\rho_i} \sum_j \frac{U_j P_i}{q_i} \boldsymbol{v}_{ij} \cdot \nabla \tilde{W}_{ij}. \tag{32}$$

Here, m_i/ρ_i is the volume associated with particle i which can be replaced by U_i/q_i. Thus, we have

$$\frac{dU_i}{dt} \simeq (\gamma - 1) \sum_j \frac{U_i U_j}{q_i} \boldsymbol{v}_{ij} \cdot \nabla \tilde{W}_{ij}, \tag{33}$$

where we used $P = (\gamma - 1)q$.

3.3. *Equation of Motion*

From the energy equation, Eq. 33, we derive the equation of motion. The change in the internal energy of particles i and j due to their relative motion is

$$\frac{dU_i}{dt} + \frac{dU_j}{dt} = (\gamma - 1) U_i U_j \left(\frac{1}{q_i} + \frac{1}{q_j} \right) \boldsymbol{v}_{ij} \cdot \nabla \tilde{W}_{ij}. \tag{34}$$

This change is the same as the change of the kinetic energy of particles with an opposite sign. Thus, we have

$$\frac{m_i m_j}{m_i + m_j} \boldsymbol{v}_{ij} \cdot \left(\frac{d\boldsymbol{v}_i}{dt} - \frac{d\boldsymbol{v}_j}{dt} \right) = -\left(\frac{dU_i}{dt} + \frac{dU_j}{dt} \right). \tag{35}$$

Substituting Eq. 34 into Eq. 35, we obtain

$$\left(\frac{d\boldsymbol{v}_i}{dt} - \frac{d\boldsymbol{v}_j}{dt} \right) = -(\gamma - 1) \frac{m_i + m_j}{m_i m_j} U_i U_j \left(\frac{1}{q_i} + \frac{1}{q_j} \right) \nabla \tilde{W}_{ij}. \tag{36}$$

Since the motion of the center of mass of two particles is unchanged by the interaction of two particle, we have

$$\frac{d}{dt}(m_i \boldsymbol{v}_i + m_j \boldsymbol{v}_j) = 0. \tag{37}$$

Thus, we have

$$m_i \frac{d\boldsymbol{v}_i}{dt} = -(\gamma - 1) U_i U_j \left(\frac{1}{q_i} + \frac{1}{q_j} \right) \nabla \tilde{W}_{ij}, \tag{38}$$

as the contribution of particle j to the equation of motion of particle i.

The equation of motion for particle i is obtained by taking summation over neighbor particles:

$$m_i \frac{d\boldsymbol{v}_i}{dt} \simeq -(\gamma - 1) \sum_j U_i U_j \left(\frac{1}{q_i} + \frac{1}{q_j} \right) \nabla \tilde{W}_{ij}. \tag{39}$$

The right-hand side of Eq. 39 contains only the energy U and energy density q. Thus, as far as q is smooth, Eq. 39 is likely to be well-behaved. The equation of motion of the standard SPH (Eq. 9) requires both P and ρ are smooth. Thus, in our formulation, there is nothing special about the contact discontinuity. We can therefore expect that the treatment of the contact discontinuity is improved. We will see this in §3.5.

Note that Eq. 39 is mathematically equivalent to the equation of motion obtained by Ritchie & Thomas (2001), while the deviation is completely different. Ritchie & Thomas (2001) started from Eq. 27 and density estimate $\rho = mq/U$, but still tried to use standard SPH estimate of Eq. 6. In order to eliminate ρ from equation of motion, they used the following formal relationship

$$\frac{\nabla P}{\rho} = \frac{\nabla P}{\rho} + \frac{P}{\rho} \nabla 1, \tag{40}$$

and formal identity

$$\nabla 1 = \sum_j m_j \frac{1}{\rho_j} \nabla W(r_{ij}, h) \simeq 0. \tag{41}$$

Thus, their deviation was a heuristic modification of the standard SPH and they did not employ the volume element U/q explicitly. We have shown that by choosing U/q as the volume element, we can derive a consistent set of SPH equations naturally.

3.4. *Artificial Viscosity*

To deal with shocks, the standard SPH needs an artificial viscosity term. Our new formulation also needs an artificial viscosity term. We utilize artificial viscosity terms which are widely used in simulations with the standard SPH.

The viscosity term for the equation of motion is

$$m_i \frac{d^2 \boldsymbol{r}_i}{dt^2} = -m_i \sum_j m_j \Pi_{ij} \nabla \tilde{W}_{ij}, \tag{42}$$

and the corresponding form of it for the energy equation is

$$\frac{dU_i}{dt} = \frac{m_i}{2} \sum_j m_j \Pi_{ij} \boldsymbol{v}_{ij} \cdot \nabla \tilde{W}_{ij}, \tag{43}$$

where Π_{ij} is the function of the strength of the artificial viscosity.

There are two types of artificial viscosity term, Π_{ij}, which are commonly used. The most commonly used one (Lattanzio et al. 1985) is

$$\Pi_{ij} = \begin{cases} \frac{-\alpha c_{ij} \mu_{ij} + \beta \mu_{ij}^2}{\rho_{ij}} & \boldsymbol{v}_{ij} \cdot \boldsymbol{r}_{ij} < 0, \\ 0 & \boldsymbol{v}_{ij} \cdot \boldsymbol{r}_{ij} \geq 0, \end{cases} \tag{44}$$

where α and β are the control parameters for the strength of the artificial viscosity, c_{ij} is the arithmetic average of the sound speeds of particles i and j, $\rho_{ij} = 0.5(\rho_i + \rho_j)$, and

$$\mu_{ij} = \frac{h_{ij} \boldsymbol{v}_{ij} \cdot \boldsymbol{r}_{ij}}{r_{ij}^2 + \epsilon h_{ij}^2}. \tag{45}$$

The constant ϵ is introduced to avoid the divergence and its fiducial value is ~ 0.01.

The other one is proposed by Monaghan (1997) from the analogy of the Riemann solver:

$$\Pi_{ij} = \begin{cases} -\frac{\alpha}{2} \frac{v_{ij}^{\rm sig} w_{ij}}{\rho_{ij}} & \boldsymbol{v}_{ij} \cdot \boldsymbol{r}_{ij} < 0, \\ 0 & \boldsymbol{v}_{ij} \cdot \boldsymbol{r}_{ij} \geq 0, \end{cases} \tag{46}$$

where $v_{ij}^{\rm sig} = c_i + c_j - 3w_{ij}$ and $w_{ij} = \boldsymbol{v}_{ij} \cdot \boldsymbol{r}_{ij} / r_{ij}$.

Since we have the density estimate $\rho = q/u$, we have

$$\rho_{ij} = \frac{1}{2} \left(\frac{q_i}{u_i} + \frac{q_j}{u_j} \right). \tag{47}$$

However, this modification of ρ_{ij} leads to unstable behavior under strong shocks. It seems to be safe to use the smoothed densities of particles i and j evaluated using Eq. 7. A consistent derivation of the artificial viscosity term in our scheme will be investigated in a forthcoming paper.

We use the standard Balsara switch (Balsara 1995) to suppress the shear viscosity. It is given by

$$F_i = \frac{|\nabla \cdot \boldsymbol{v}_i|}{|\nabla \cdot \boldsymbol{v}_i| + |\nabla \times \boldsymbol{v}_i| + \epsilon_b c_i / h_i}, \tag{48}$$

and $\Pi_{ij,\rm Balsara} = 0.5(F_i + F_j)\Pi_{ij}$. Here ϵ_b is a small value (typically 10^{-4}). The rotation of velocity in the standard SPH is found in literature (e.g., Monaghan 1992). The rotation of velocity in our SPH is calculated as follows:

$$\nabla \times \boldsymbol{v}_i \simeq \frac{1}{q_i} \sum_j U_j \boldsymbol{v}_{ij} \times \nabla W(r_{ij}, h_i). \tag{49}$$

3.5. *Pressure in Contact Discontinuities*

The pressure around the contact discontinuity calculated with our SPH equation is shown in the bottom panels of figure 1. In the case of the equal-mass particle and the fixed neighbor number (the left panel), we can see that the jump of the pressure at the contact discontinuity in our SPH is much smaller than that in the standard SPH. In the case of the constant kernel size (the middle panel), the result of our SPH is almost flat, while that of the standard SPH has a large error.

In these two equal-mass cases, pressure still has small jumps at the contact discontinuity. The reason is that in both cases the distribution of particles is asymmetric. In the high-density region, the particle separation is smaller, resulting in small integration error. As a result, small error appears when the kernel contains the contribution from both low- and high-density regions. In the case of the equal separation of particles, there is no jump in the pressure distribution at the contact discontinuity, as shown in the rightmost panel.

4. NUMERICAL EXPERIMENTS

In this section, we show the results of several standard tests for fluid schemes, for both the standard SPH and our new SPH. In §4.1, we describe our numerical code briefly. In §4.2, we show the results of the shock tube tests. Then we show the evolution of system which is initially in hydrostatic equilibrium in §4.3. In §4.4 and §4.5, tests for two important fluid instabilities are carried out. Finally, we show the results of the blob tests which was first proposed by Agertz et al. (2007). In all tests, our new SPH shows much better result compared to that of the standard SPH.

4.1. *Numerical Method*

We used `ASURA`, a parallel N-body/SPH code, as a framework of current numerical experiments. `ASURA` adopts the leap-frog method for the time-integration. For simplicity, we used the shared steps with variable time-steps. The time-step is given by

$$dt = \min_i dt_i, \tag{50}$$

where

$$dt_i = C_{\rm CFL} \frac{2h_i}{\max_j v_i^{\rm sig}}, \tag{51}$$

and $C_{\rm CFL} = 0.3$.

For the standard SPH, we first evaluated the densities of particles using Eq. 16. Then, we calculated the pressure gradient and the time-derivative of the internal energy using Eqs. 17 and 18. In our new SPH, we evaluated q using Eq. 27 first, and then we calculated the pressure gradient and the time derivative of the internal energy using Eqs. 39 and 33. We used Eq. 46 as the artificial viscosity term in both cases and we adopted $\alpha = 1$. The Balsara switch was also applied. To avoid the tensile instability, we used a first derivative of the kernel which has a cuspy core (Thomas & Couchman 1992).

The kernel size of each particle is determine to keep the number of neighbor particles within the range of 32 ± 2. As an exception, in the one dimensional tests shown in §4.2, the kernel size is evaluated by

$$h = \eta \left(\frac{m}{\rho} \right), \tag{52}$$

or

$$h = \eta \left(\frac{mu}{q} \right), \tag{53}$$

where $\eta = 1.2$ for the Sod's shock tube tests and $\eta = 2.4$ for the strong shock tube tests.

For brevity, we sometimes express the standard SPH as SSPH.

4.2. *Shock Tube Tests*

The Sod shock tube (Sod 1978) is the most basic test for numerical schemes for compressible fluid. This test shows the shock capturing ability of schemes. In SPH, not only the profile of the shock front but also the behavior of the contact discontinuity is important. Here, we show the results of one- and three-dimensional shock tube tests.

The setup is as follows. We prepared the periodic domain of $-1 \leq x < 1$ for the one-dimensional tests and $-1 \leq x < 1$, $-1/16 \leq y < 1/16$, and $-1/16 \leq z < 1/16$ for the three dimensional tests. The initial condition is given by

$$\begin{cases} \rho = 1, P = 1, v = 0, & x < 0, \\ \rho = 0.25, P = 0.1795, v = 0, & x \geq 0. \end{cases} \tag{54}$$

To express this initial condition, we use equal-mass particles and place 800 and 200 particles in the left and right domains, respectively, regularly in the one-dimensional tests. In three dimensional tests, we place 40000 and 10000 particles in the left and right domains, respectively, and a glass-like particle distribution was used. We set $\gamma = 1.4$ and gave the internal energy to each particle to ensure the given P.

In addition to the Sod shock tube, we performed a one-dimensional strong shock test. The initial condition for this test is given by

$$\begin{cases} \rho = 1, P = 1000, v = 0, & x < 0, \\ \rho = 1, P = 0.01, v = 0, & x \geq 0. \end{cases} \tag{55}$$

We use 1000 equal-mass particles in the computational domain of $-1 \leq x < 1$ with the equal separation.

Figure 2 shows the results of the one-dimensional shock tube tests with the standard SPH and our new SPH. The density (upper row) and pressure (bottom row) of each particle are plotted by circles. The red curves represent the analytic solutions.

The standard SPH reproduce the analytic solution of the density distribution well. The shock front is resolved by ~ 7 particles. The jump of the density at the contact discontinuity is resolved by a similar number of particles. The pressure shows large variations near the contact discontinuity, though it should be constant. Since Eq. 9 of the standard SPH contains a large error near the contact discontinuity, in order to achieve zero acceleration, pressures of particles must have large variations. This result is the same as the results of previous works with the standard SPH (e.g., Springel 2005; Price 2008).

In our new SPH, unlike the case of the standard SPH, the pressure around the contact discontinuity does not show a large jump. The reason is simply that the energy density is used instead of the mass density. The energy density is constant at the contact discontinuity. The reason why there is a small change in the pressure is that

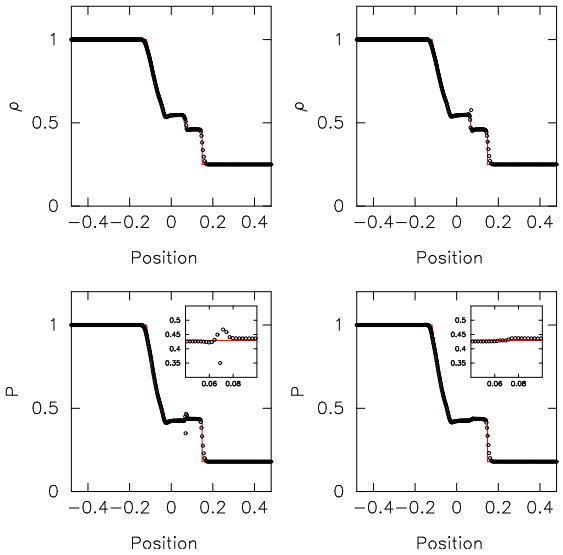

FIG. 2.— The results of the one dimensional shock tube tests for SSPH and our new SPH at $t = 0.1$. Density (upper row) and pressure (bottom row) are shown. Circles indicate the physical quantities of each SPH particle, while red curves represent the analytic solutions. Insets in the pressure panels are the close-up views around the contact discontinuity.

the particle separation changes at the contact discontinuity. As we showed in figure 1, our new SPH still has small error in the pressure, due to the finite number of particles in the kernel. This error caused the change in the pressure in figure 2.

The results of the three dimensional shock tube tests for the standard SPH and our SPH are shown in figure 3. In this figure, the circles represent average values of particles in bins with the width of the mean particle separation at the high density part. Again, we can see a variation in the pressure around the contact discontinuity in the case of the standard SPH. In the case of our SPH, there is no such variation.

Figure 4 shows the results of the strong shock tube tests for the standard SPH and our new SPH. The shock front and the contact discontinuity in the density distribution is well reproduced in the both cases. In this extreme test, both runs show jumps in the pressure distribution around the contact discontinuity. The absolute value of the pressure jump in our SPH is much smaller than that in the standard SPH. The jump found in the pressure in our SPH is caused by the asymmetry in the particle distribution (see §3.5). Overall, our SPH can handle such a strong shock problem, even when a very large pressure jump exists initially. This result is quite reassuring. In our new SPH, it is assumed that pressure is continuous, which is not a valid assumption at the shock front. Thus, it could fail to capture very strong shocks. The result shown in figure 4 shows that is not the case and our new SPH can handle very strong shocks.

4.3. *Hydrostatic Equilibrium Tests*

As is shown in §2, in the standard SPH, particles feel *unphysical repulsive force* at the interface of the contact discontinuity. Therefore, in order to establish the hydrostatic equilibrium, the distance between particles at the different sides of the contact discontinuity must become larger than the "true" value. What is the consequence of

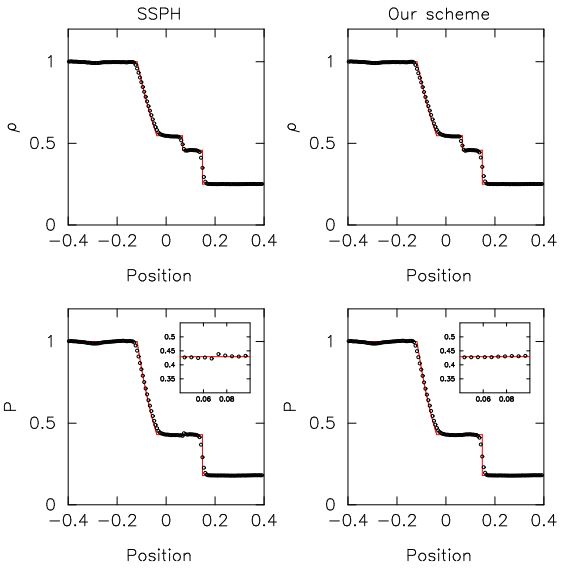

FIG. 3.— The results of the three dimensional shock tube tests for SSPH and our new SPH at $t = 0.1$. Density (upper row) and pressure (bottom row) are shown. Circles indicate the averaged physical quantities of SPH particles, while red curves represent the analytic solutions.

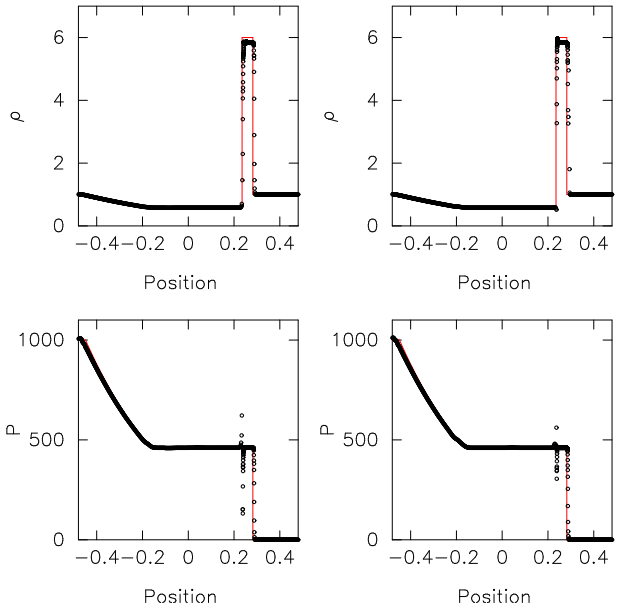

FIG. 4.— The same as figure 2, but for the strong shock tube tests at $t = 0.012$.

this repulsive force? Here, we show the result of a simple test which helps us to understand the problem of the unphysical repulsive force. Similar test has been used in Heß & Springel (2010).

We follow the evolution of two fluids with different values of density, but with the same pressure. We performed two-dimensional tests. The computational domain is a square of the unit size, $0 \le x < 1$ and $0 \le y < 1$, with a periodic boundary condition. Initial conditions are

$$\rho = \begin{cases} 4 & 0.25 \le x \le 0.75 \text{ and } 0.25 \le y \le 0.75, \\ 1 & \text{otherwise}, \end{cases} \quad (56)$$

$$P = 2.5, \quad (57)$$

$$\gamma = 5/3. \quad (58)$$

We tried two different realizations. In the first one, the particle mass is the same for the entire computational region. Thus, the inter-particle distance is smaller in the high density region. In the second one, particles in the high density region is four times more massive than particles in the low-density region. In both cases, particles are initially in a regular grid. For the equal-mass case, the number of particles in the dense region is 4096 and that in the ambient is 3072. For the equal-separation cases, those are 1024 and 3072, respectively. Initial velocities of particles were set to zero. Since the system is initially in the hydrostatic equilibrium, particles should not move, except for small local adjustments.

Figure 5 shows the time evolution up to $t = 8$. There is a clear difference between the result of the standard SPH and that of our SPH. With the standard SPH, the high-density region, which initially has a square shape, quickly becomes rounder and almost completely circular by $t = 8$. We can understand this unphysical rounding as follows. As we stated in §2 and §3.5, unphysical repulsive force between particles operates at the contact discontinuity. We can see the effect of this force in the development of the gap of the distribution of particles near the boundary of two fluids. Because of this gap, the bulk of the system is slightly compressed. The system seeks to achieve the energy minimum, by minimizing the surface area of the contact discontinuity. Thus, the high-density region evolves to a circular shape, which minimizes the length of the boundary. In other words, the repulsive force effectively adds the "surface tension".

Our new SPH gives a far better solution, as we can see in the lower two rows of figure 5. The overall square shape remains there till the end of the simulation in the equal-mass case. The result of the unequal-mass case is even better. The equation of motion of our SPH eliminates the unphysical surface tension completely.

Figure 6 shows the final state of the two-fluid system with the density contrast of 64. Our SPH handles the system without any problem (right panel). On the other hand, in the calculation with the standard SPH, a wide and empty ring structure is formed between two fluids.

4.4. *Kelvin-Helmholtz Instability Tests*

After the work by Agertz et al. (2007) which demonstrated clearly that the standard SPH cannot deal with the Kelvin-Helmholtz instability correctly, many researchers proposed modifications of SPH to solve the problem (see §1). In this section, we investigate how our new SPH handles the Kelvin-Helmholtz instability.

We prepared a two-dimensional computational domain, $0 \le x < 1$ and $0 \le y < 1$. The periodic boundary condition was used. The density is

$$\rho = \begin{cases} 1(\equiv \rho_l) & 0 \le y < 0.25,\ 0.75 \le y < 1, \\ 2(\equiv \rho_h) & 0.25 \le y < 0.75. \end{cases} \quad (59)$$

We used equal-mass particles. The numbers of particles in the high and low dense regions are 131072 and 65522,

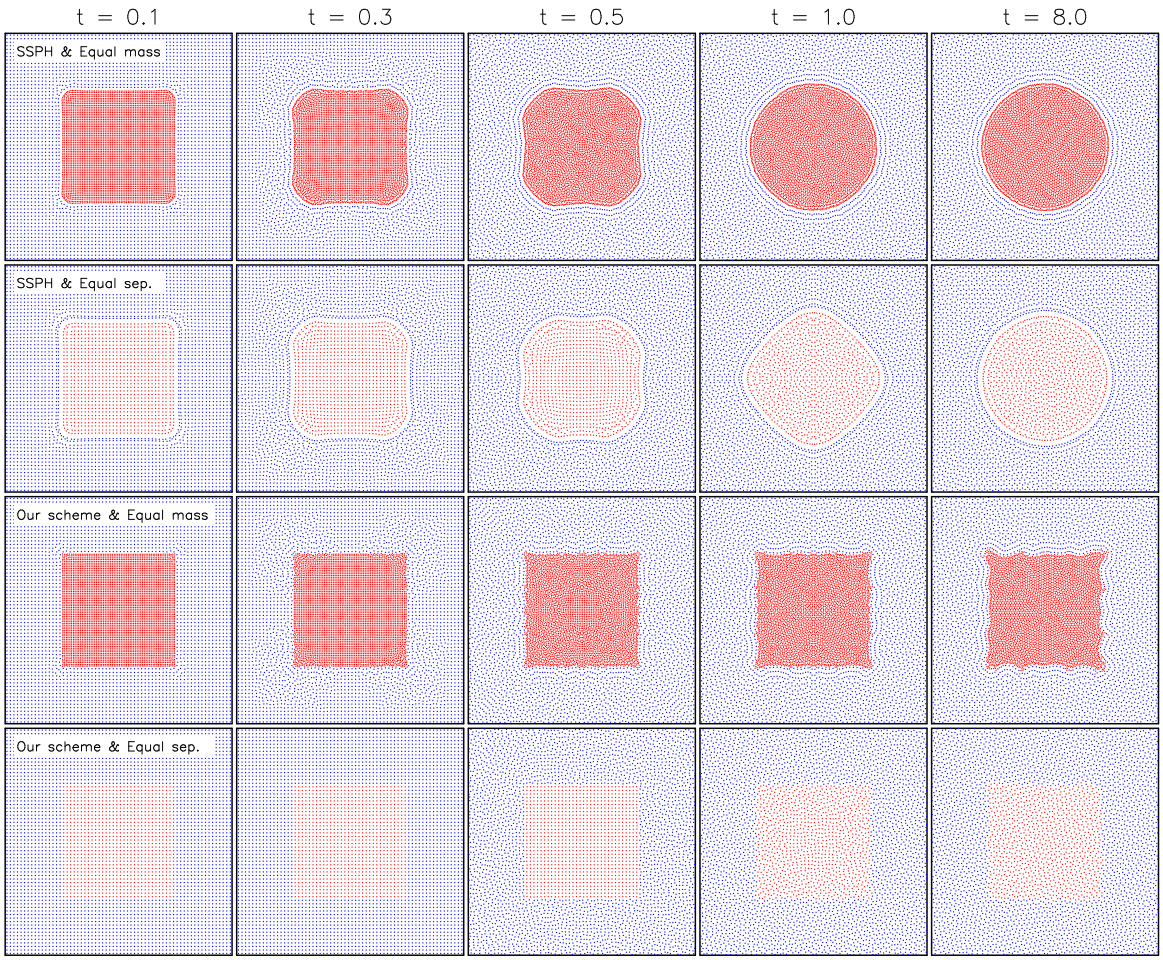

FIG. 5.— Snapshots of a two-fluid system at $t = 0.1$, 0.3, 0.5, 1 and 8. The red and blue points indicate the positions of particles with $\rho = 4$ and $\rho = 1$, respectively. The upper two rows are the results of SSPH, while the lower two rows are those of our SPH. The first and third rows show the results of the equal-mass cases, whereas the second and fourth rows show those of the equal separation and unequal mass cases.

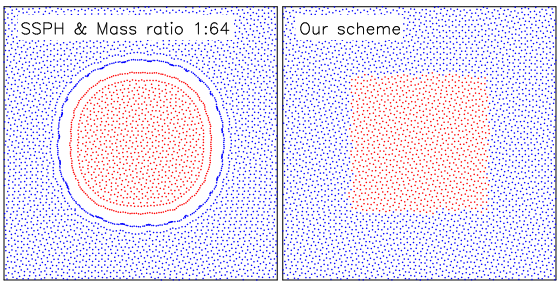

FIG. 6.— The final state ($t = 8$) of a two fluid system with the density contrast of 64. The red and blue points are the positions of particles with $\rho = 64$ and 1, respectively. The particle separation is constant and the particle mass difference is 1:64.

respectively. We set $P = 2.5$ and $\gamma = 5/3$. The high and low density regions had the initial velocities of $v_{x,h} = 0.5$ and $v_{x,l} = -0.5$ in the x direction, respectively.

We have used $N_{\rm nb} = 32 \pm 2$ as the neighbor number. This value might seem a bit large, but we found it guarantees the good sampling of the particles in the low-density region at the interface. When we used $N_{\rm nb} = 16 \pm 2$, the variation of the pressure at the interface becomes too large. For the artificial viscosity, we used $\alpha = 1$ with the Balsara switch.

We added a small velocity perturbation to the particles near the interfaces, following Price (2008). The velocity perturbation in the y direction is as follows:

$$\Delta v_y = \begin{cases} A\sin[-2\pi(x+0.5)/\lambda], & |y-0.25| < 0.025 \\ A\sin[2\pi(x+0.5)/\lambda], & |y-0.75| < 0.025, \end{cases} \tag{60}$$

where $\lambda = 1/6$ and $A = 0.025$.

The time-scale of the growth of the Kelvin-Helmholtz instability is

$$\tau_{\rm kh} = \frac{\lambda(\rho_h + \rho_l)}{\sqrt{\rho_h \rho_l}|v_{x,h} - v_{x,l}|}. \tag{61}$$

For our test setup, $\tau_{\rm kh} = 0.35$. We followed the evolution up to $t = 8\tau_{\rm kh}$.

The results are shown in figure 7. The difference between two results is clear. In the run with the standard SPH, perturbations grow till $t = \tau_{\rm kh}$, but the unphysical surface tension inhibited the growth of roll-like structures. The stretched high-density fluids break apart ($t = 4\tau_{\rm kh}$) and form blobs ($t = 8\tau_{\rm kh}$). This evolution is completely different from those obtained by Euler codes (e.g., Agertz et al. 2007). On the other hand, our new SPH shows a very good result which is comparable to those with Euler codes and with SPH with the Ritchie & Thomas (2001) equation of motion or the artificial conductivity (see Price 2008).

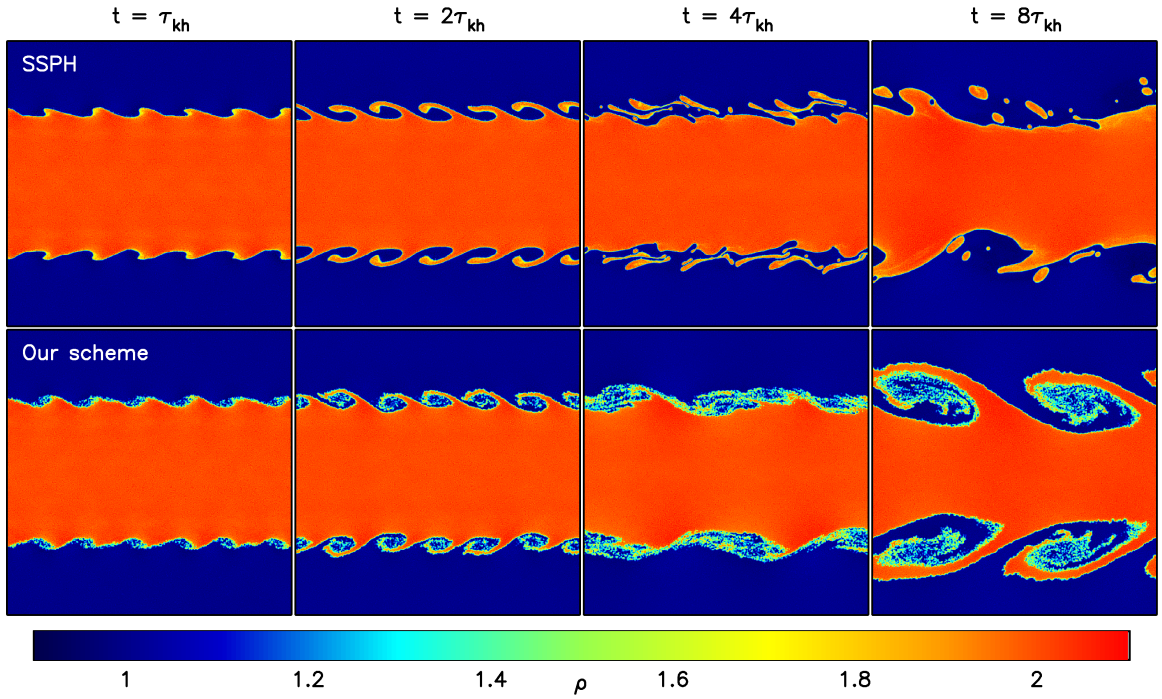

FIG. 7.— The density maps from the two dimensional shear flow test at $t = 1, 2, 4$ and 8 $\tau_{\rm kh}$. The upper panels show the results of SSPH, while the bottom panels show those of our SPH. The color code of the density is given at the bottom.

Figure 8 shows the cross section of the pressure distribution along the y-axis. We can see that a very large pressure jump exists around the contact interfaces, in the case of the standard SPH. The surface tension at the interface of the two fluids prevents the normal growth of the Kelvin-Helmholtz instability. On the other hand, there is no such jump in the case of our SPH. Since the pressure and particle distribution is well-behaved at the interface, the growth of the Kelvin-Helmholtz instability is not suppressed.

4.5. *Rayleigh-Taylor Instability Tests*

Abel (2011) demonstrated that the standard SPH cannot follow the development of the Rayleigh-Taylor instability correctly. We show the result with our SPH as well as that with the standard SPH.

The initial setup is as follows. We prepared the two dimensional computational domain of $0 \le x < 1$ and $0 \le y < 1$. We placed two fluids separated at $y = 0.5$. The density just above (below) the interface was set to $\rho_h \equiv 2$ ($\rho_l \equiv 1$). These two fluids were initially in the hydrostatic equilibrium. Further, we assumed that each fluid was initially isoentropic. The density distributions of these fluids in the vertical direction are given by

$$\rho = \begin{cases} \rho_l \left[1 + \frac{\gamma-1}{\gamma}\frac{\rho_l g(y-0.5)}{P_0}\right]^{\frac{1}{\gamma-1}} & y < 0.5, \\ \rho_h \left[1 + \frac{\gamma-1}{\gamma}\frac{\rho_h g(y-0.5)}{P_0}\right]^{\frac{1}{\gamma-1}} & y \ge 0.5, \end{cases} \tag{62}$$

where $g = -0.5$ is the gravitational constant, $P_0 = 10/7$ is the value of pressure at the interface, and $\gamma = 1.4$. The initial density and entropy profiles are shown in figure 9. To ensure the initial density distribution given by Eq. 62, we first placed equal-mass particles on the regular grid with the separation of 1/512. Then, we adjusted the vertical separation of each particle set having the same y to reproduce the density distribution. The particle mass was set to 5.7×10^{-6} and the total number of particles was 247296. The periodic boundary condition was imposed on the x direction. Particles with $y < 0.1$ and $y > 0.9$ were fixed at the initial positions and they were not allow to change their internal energy.

The velocity perturbation in the vertical direction was added as the seed of the instabilities. We carried out runs with two kinds of the seed. For the first test, we added the velocity perturbation to particles in the range of $0.3 < y < 0.7$, and the form of the perturbation is

$$\Delta v_y(x, y) = \delta_{vy}[1+\cos(4\pi x)]\{1+\cos[5\pi(y-0.5)]\}. \tag{63}$$

We set $\delta_{vy} = 0.025$. For the second test, we added the velocity perturbation of the form:

$$\Delta v_y(x, y) = \sum_{j=20}^{40} a_j \frac{n_j}{k_j} \cos(k_j x) \exp(-0.05 k_j |y - 0.5|), \tag{64}$$

and

$$n_j^2 = k_j |g| \left(\frac{\rho_h - \rho_l}{\rho_h + \rho_l}\right), \tag{65}$$

where n_j is the linear growth rate of the Rayleigh-Taylor instability, and $k_j = j\pi/L(\equiv 1)$ is the wave number of the perturbation. The amplitude of each mode, a_j, was drawn from a Gaussian distribution with the variance of unity at random. This initial velocity perturbation is based on Youngs (1984) with slight modifications. Velocities of the particles outside the perturbed region was set to zero. We call these two tests single-mode and multi-mode tests, respectively.

In figure 10, the growth of the Rayleigh-Taylor instability in the case of the single-mode test is shown. The Rayleigh-Taylor instability develops in calculations with both of the standard SPH and our SPH, but the structures of them are quite different. The unphysical surface

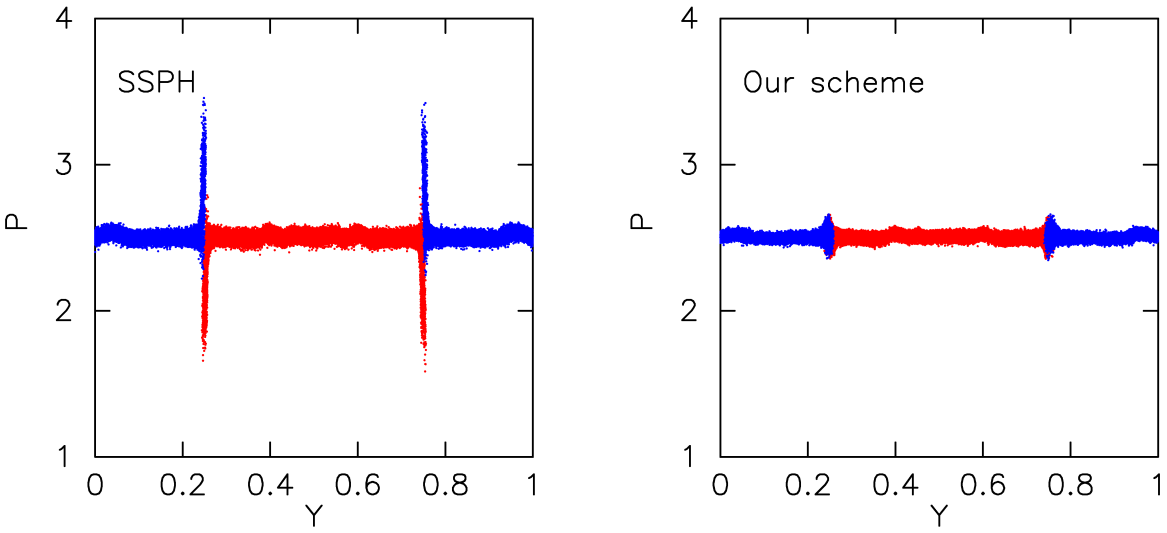

FIG. 8.— Pressure of each particle along the y direction at $t = 0.4\ \tau_{kh}$. The left panel shows the result of SSPH, whereas the right panel shows that of our SPH. Particles initially in the high- (low-) density region are expressed with red (blue) points.

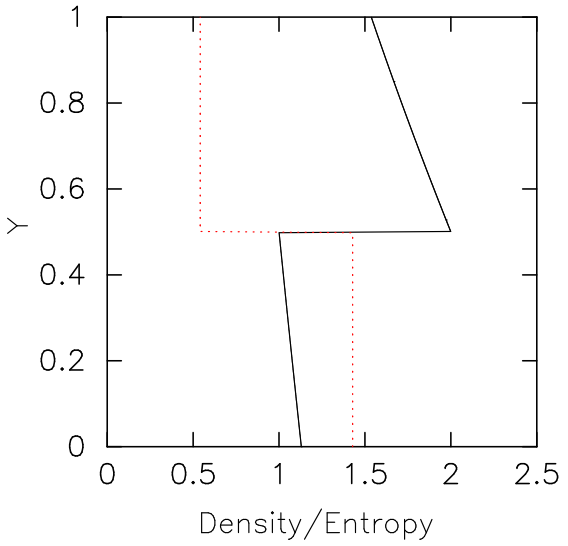

FIG. 9.— Initial distributions of density and entropy in the vertical direction. Solid and dotted curves indicate density and entropy, respectively.

tension of the standard SPH again prevents the development of the fine structures on the surface of the Rayleigh-Taylor fingers. Thus, the result looks quite different from those obtained with Euler schemes. On the other hand, in the calculation with our SPH, the overall evolution of the Rayleigh-Taylor instability in our SPH shows excellent agreement with those with Euler schemes and the moving mesh scheme (see Springel 2010a).

Figure 11 shows the growth of the Rayleigh-Taylor instability with the multi-mode perturbations with the standard SPH and our new SPH. The global phase mixing of fluids can be seen in the result with our SPH. On the other hand, due to the unphysical surface tension, the mixing is significantly suppressed in that of the standard SPH. The distribution of two fluids looks like a mixture of oil and water.

4.6. *Blob Tests*

As the final test, we performed the blob test proposed by Agertz et al. (2007). This test incorporates both the Kelvin-Helmholtz and Rayleigh-Taylor instabilities.

We used Read's initial condition of the blob test (Read et al. 2010; Read & Hayfield 2011) [2]. The computational domain was $0 \leq x < 2000$ kpc, $0 \leq y < 2000$ kpc, and $0 \leq z < 6000$ kpc, and the periodic boundary condition was imposed. A cold cloud of the density $\rho_c = 3.13 \times 10^{-7}$ in the mass unit of $2.3 \times 10^5 M_\odot$and the length unit of 1 kpc and temperature $T_c = 10^6$K was centered at $(x, y, z) = (1000\ \mathrm{kpc}, 1000\ \mathrm{kpc}, 2000\ \mathrm{kpc})$. The radius of this cloud was 197 kpc. This cloud was embedded in the diffuse ambient gas of which density and temperature were $\rho_a = 3.13 \times 10^{-8}$ and $T_a = 10^7$ K, respectively. The ambient gas had the velocity of $v_z = 1000$ kms^{-1}. Thus, the Mach number of the flow to the cloud was 2.7. The total number of particle for the system is 4643283. We integrated the system up to $t = 5\tau_{\rm kh}$, where $\tau_{\rm kh} = 2$ Gyr is the typical growth time-scale of the Kelvin-Helmholtz instability in this test (Agertz et al. 2007).

Figure 12 shows the snapshots of the cloud core. The upper and lower panels are the results with the standard SPH and our SPH, respectively. Their evolutions were quite different. The blob simulated with the standard SPH retained the single cloud structure until the late stage of the simulation. This behavior is consistent with those with the standard SPH shown in Agertz et al. (2007). In contrast, the blob surface was disrupted in the run with our SPH, due to the growth of the instabilities on the surface. The blob fragmented into several peaces and mixed eventually with the ambient gas. This behavior is similar to those obtained by Euler codes.

The evolution of the blob mass is shown in figure 13. Here we show the mass of gas with $\rho > 0.64\ \rho_c$ and $T < 0.9\ T_a$, following Agertz et al. (2007). At $t = 2.5\ \tau_{\rm kh}$, the blob mass in the run of our SPH became ~ 10 % of the initial mass. This result is consistent with the results of the Euler codes (see figure 6 in Agertz et al. 2007). The evolution of the blob mass in the standard SPH was

[2] We obtained the initial condition from the following URL: http://www-theorie.physik.uzh.ch/astrosim/code/

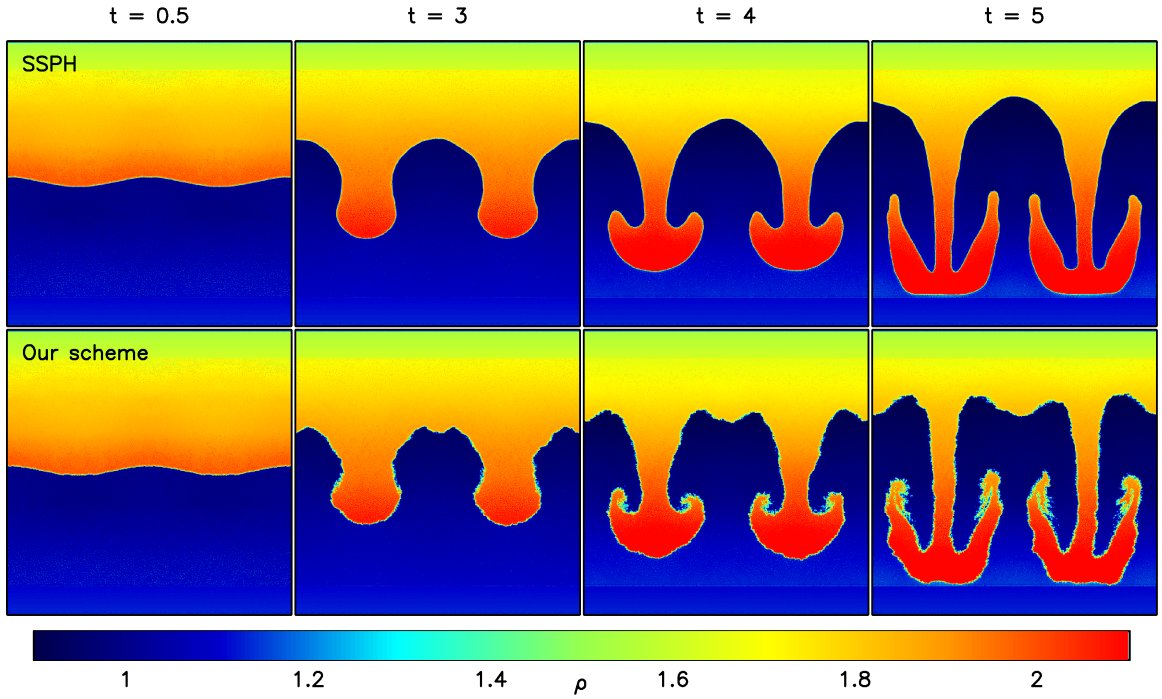

FIG. 10.— The density maps of the two dimensional Rayleigh-Taylor instability tests at $t = 0.5, 3, 4$ and 5. The upper panels show the results of SSPH, while the bottom panels show those of our SPH. The color code of the density is given at the bottom.

much slower compared to that in our SPH.

5. SUMMARY AND DISCUSSION

In this paper, we described an alternative formulation of SPH in which the energy density is used as the basis of the smoothing instead of the mass density. In our formulation, the mass of particles is not used in the evaluation of the right-hand sides of the energy equation and the equation of motion. As a result, the large error of force estimate at the contact discontinuity, which is unavoidable with the standard SPH, disappears completely in our SPH. Not surprisingly, our SPH can handle contact discontinuities and the Kelvin-Helmholtz and Rayleigh-Taylor instabilities without difficulty. The behavior of the shock in our new SPH is essentially the same as that in the standard SPH. Since the equations used in our SPH are almost identical to those of in the standard SPH except that energy density is used in place of mass density ρ. Modification of existing SPH code to use our scheme is simple and straightforward. In particular, there is no increase in the calculation cost. Equations which are not derived in this paper, such as the diffusion equation (Brookshaw 1985), can be derived easily.

Price (2008) improved the treatment of the Kelvin-Helmholtz instability of the standard SPH, by applying artificial conductivity at the contact discontinuity. Unlike the artificial viscosity, artificial conductivity introduces the dissipation not in the original set of equation. Our SPH does not need such additional dissipation, and thus the contact discontinuity is kept sharp.

One might think our result contradicts with the requirement that all quantities in SPH must be smooth (Monaghan 1997). However, it is obvious that in our SPH, all quantities in the right-hand side of the equations are smooth, since the only discontinuous quantity is the density and it does not appear in the right-hand sides. Thus, our results does not contradict with Monaghan's requirement.

In this paper,we discuss the treatment of ideal gas only. We are currently working on the extension to non-ideal fluid, and the result will be given in the forthcoming paper.

Some of the numerical tests were carried out on the Cray XT4 system in the Center for Computational Astrophysics at the National Astronomical Observatory of Japan. This work is supported by HPCI Strategic Program Field 5 'The origin of matter and the universe' and Grant-in-Aid for Scientific Research (21244020) of Japan Society for the Promotion of Science, Ministry of Education, Culture, Sports, Science and Technology, Japan.

REFERENCES

Abel, T. 2011, MNRAS, 413, 271
Agertz, O., et al. 2007, MNRAS, 380, 963
Balsara, D. S. 1995, Journal of Computational Physics, 121, 357
Brookshaw, L. 1985, Proceedings of the Astronomical Society of Australia, 6, 207
García-Senz, D., Cabezón, R. M., & Escartín, J. A. 2012, A&A, 538, A9
Gingold, R. A., & Monaghan, J. J. 1977, MNRAS, 181, 375
Hernquist, L., & Katz, N. 1989, ApJS, 70, 419
Heß, S., & Springel, V. 2010, MNRAS, 406, 2289
Lattanzio, J. C., Monaghan, J. J., Pongracic, H., & Schwarz, M. P. 1985, MNRAS, 215, 125
Liu, G. R., & Liu, M. B. 2003, Smoothed particle hydrodynamics: a meshfree particle method (World Scientific Publishing Company)
Lucy, L. B. 1977, AJ, 82, 1013
Monaghan, J. J. 1992, ARA&A, 30, 543
—. 1997, Journal of Computational Physics, 136, 298

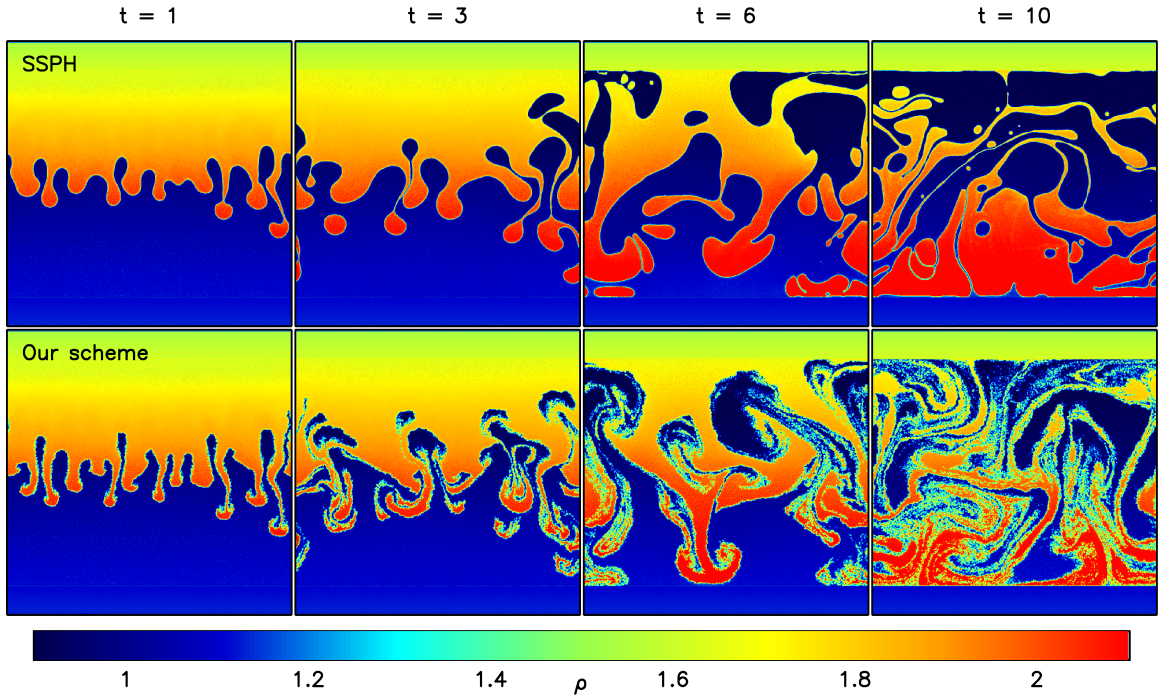

FIG. 11.— The same as figure 11, but for the multi-mode perturbations.

—. 2005, Reports on Progress in Physics, 68, 1703
Okamoto, T., Jenkins, A., Eke, V. R., Quilis, V., & Frenk, C. S. 2003, MNRAS, 345, 429
Price, D. J. 2008, Journal of Computational Physics, 227, 10040
Read, J. I., & Hayfield, T. 2011, ArXiv e-prints
Read, J. I., Hayfield, T., & Agertz, O. 2010, MNRAS, 405, 1513
Ritchie, B. W., & Thomas, P. A. 2001, MNRAS, 323, 743
Rosswog, S. 2009, New Astron. Rev., 53, 78
Sod, G. A. 1978, Journal of Computational Physics, 27, 1
Springel, V. 2005, MNRAS, 364, 1105
—. 2010a, MNRAS, 401, 791
—. 2010b, ARA&A, 48, 391
Thomas, P. A., & Couchman, H. M. P. 1992, MNRAS, 257, 11
Youngs, D. L. 1984, Physica D Nonlinear Phenomena, 12, 32

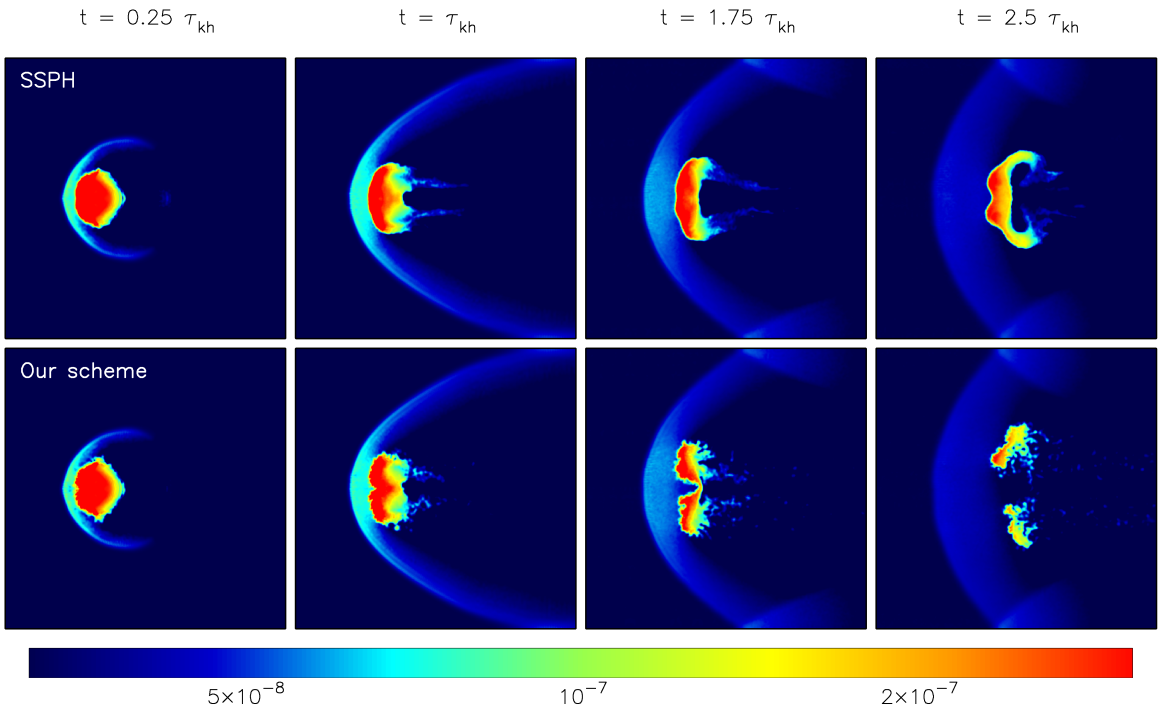

FIG. 12.— The density maps at $t = 0.25$, 1.0, 1.75 and 2.5 $\tau_{\rm kh}$. The upper and lower panels show the results with SSPH and our SPH, respectively. The color code of the density is given at the bottom.

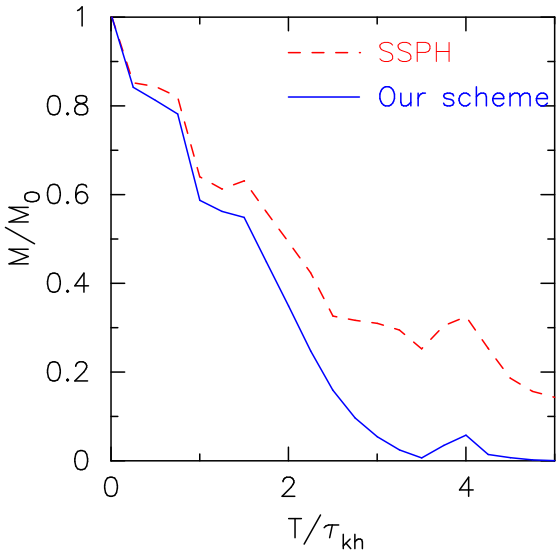

FIG. 13.— The evolution of the blob mass up to $t = 5$ $\tau_{\rm kh}$.